Journal of Magnetic Resonance 196 (2009) 142–148

Contents lists available at ScienceDirect

Journal of Magnetic Resonance

journal homepage: www.elsevier.com/locate/jmr

Magnetic resonance velocity imaging of liquid and gas two-phase flow in packed beds

M.H. Sankey, D.J. Holland, A.J. Sederman, L.F. Gladden *

Department of Chemical Engineering and Biotechnology, University of Cambridge, Pembroke Street, Cambridge CB2 3RA, UK

ARTICLE INFO

Article history:
Received 10 August 2008
Revised 30 October 2008
Available online 14 November 2008

Keywords:
Magnetic resonance imaging
Two-phase flow
Hydrodynamics
Porous media
Reaction engineering

ABSTRACT

Single-phase liquid flow in porous media such as bead packs and model fixed bed reactors has been well studied by MRI. To some extent this early work represents the necessary preliminary research to address the more challenging problem of two-phase flow of gas and liquid within these systems. In this paper, we present images of both the gas and liquid velocities during stable liquid–gas flow of water and SF_6 within a packing of 5 mm spheres contained within columns of diameter 40 and 27 mm; images being acquired using ^1H and ^{19}F observation for the water and SF_6, respectively. Liquid and gas flow rates calculated from the velocity images are in agreement with macroscopic flow rate measurements to within 7% and 5%, respectively. In addition to the information obtained directly from these images, the ability to measure liquid and gas flow fields within the same sample environment will enable us to explore the validity of assumptions used in numerical modelling of two-phase flows.

1. Introduction

The most common three-phase reactor in industry is the trickle-bed reactor, which is a reactor in which the gas and liquid phases flow co-currently down through a fixed bed of solid particles. In many applications the solid particles will be catalyst pellets. These reactors are used extensively in the petrochemical, biochemical and waste treatment industries [1] employing a wide range of operating conditions, including some similar to those used in the present work. The performance of a trickle-bed reactor is inextricably linked to the flow fields of the fluids within it. Until the advent of tomographic and MRI techniques only global properties of these systems could be determined. Such measurements include gas and liquid flow rates, pressure drop across the bed, liquid holdup, wetting efficiency, axial dispersion coefficient and residence time [2]. While global properties of the hydrodynamics are useful, they cannot in themselves give a complete picture of the performance of the reactor because the inhomogeneity of the packing structure causes significant local variations in holdup, wetting and fluid velocities.

In addition to imaging the gas and liquid distribution in the bed, MRI allows us to acquire non-invasive measurements of the local flow velocities within the bed. These data can be used in two distinct ways. First, by imaging the local hydrodynamics we may be able to explore how liquid and gas velocities adjacent to a catalyst pellet influence the catalytic conversion within the pore space of the pellet. Second, images of the local hydrodynamics under conditions of two-phase flow will allow us to assess the accuracy and appropriateness of assumptions and closure laws used in the numerical modelling of hydrodynamics within these reactors. In the present work we report the implementation of MRI experiments to enable such measurements to be made, along with the first report of liquid and gas velocity maps recorded from the same sample environment.

Previous MRI studies of two-phase flow in fixed-bed reactors include MRI visualisations of liquid distribution when the reactor is operating in the trickle-flow regime [3–5]; the trickle-flow regime is defined as being when the distribution of gas and liquid within the bed is stable with time. More recent studies [6,7] have acquired images of liquid distribution and used these data to compare with predictions of liquid holdup and static liquid saturation. Developments in ultra-fast MRI have also enabled the real-time visualisation of pulsing flow, which occurs at higher liquid velocities which causes liquid pulses to form and move through the bed. Lim et al. [8] used the FLASH technique to acquire two-dimensional (2D) images of the liquid distribution in this flow regime. This work was extended using three-dimensional (3D) FLASH to give insights into the mechanism of the hydrodynamic transition from trickle to pulsing flow [9,10]. In all cases, the aforementioned experiments have imaged the spatial distribution of the liquid phase and inferred the distribution of the gas phase. Velocity imaging of neither phase has been reported.

Previous reports of imaging thermally polarised gases in reaction engineering systems include ^1H imaging of thermally polarised acetylene, propane and butane flowing in monolithic

* Corresponding author.
E-mail address: Gladden@cheng.cam.ac.uk (L.F. Gladden).

1090-7807/$ - see front matter © 2008 Elsevier Inc. All rights reserved.
doi:10.1016/j.jmr.2008.10.021

alumina catalysts [11] and ^{19}F purely phase encode imaging of highly turbulent gas flow [12]. We also note for completeness that the combination of ^{1}H and ^{19}F imaging to study dynamic multiphase systems has also been employed by Beyea et al. [13]. In that work, ^{19}F spin-echo imaging of a polytetrafluoroethylene oil was interlaced with ^{1}H SPRITE imaging of low-density polyethylene particles to investigate sedimentation in a solid–solid–liquid system.

This paper reports the first measurements of local liquid and gas velocity in a trickle-bed reactor. Since no reaction is occurring, the system under study is more correctly referred to as a fixed bed. Indeed when spherical, non-porous packing elements are used, the system is purely a porous medium comprising a packing of spheres. The gas and liquid are supplied to the packing at flow rates such that the spatial distribution of the gas and liquid remains constant with time; i.e., we are operating in the trickle-flow regime.

To achieve gas velocity measurements, SF_6 gas has been used because it has particularly favourable MR characteristics. In addition to the high gyromagnetic ratio (γ) of ^{19}F and the large number of ^{19}F nuclei per molecule, SF_6 has a relatively low self-diffusion coefficient (D). For example, $D = 3.45 \times 10^{-6}\,m^2\,s^{-1}$ at 1 bar and 20 °C [14], nearly an order of magnitude less than other common gases. Here, and throughout the rest of the paper, pressures are quoted as absolute values (not gauge) and in units of bar equivalent to 10^5 Pa. A relatively low self-diffusion coefficient reduces diffusive attenuation in the presence of magnetic field gradients, and also reduces diffusive blurring, thereby improving image resolution. Further, SF_6 has short relaxation times. At atmospheric pressure $T_1 = T_2 = 2.0$ ms [15]. This allows many signal averages per unit time (e.g. at least 100 times more than propane), thus improving the signal-to-noise ratio. However, low values of T_2 make it difficult to implement velocity measurements for moderate velocities, say <1 m s^{-1}, because of the limit to the maximum value of the observation time Δ that can be employed. In the present work, SF_6 is pressurised; this has three benefits. First, it increases the spin density in direct proportion to the pressure, thereby enhancing MR sensitivity. Second, the molecular self-diffusion coefficient decreases in inverse proportion to P; this reduces diffusive attenuation and blurring. Third, the relaxation times of ^{19}F in SF_6 increase approximately linearly with P; this allows the successful implementation of spin-echo velocity imaging pulse sequences capable of measuring velocities down to $\sim$cm s^{-1}.

2. Experimental

2.1. Apparatus

Gas and liquid were flowed co-currently downwards in two different packed beds. The first was a wide glass column with internal diameter 40.0 (±0.2) mm and length 50.0 cm. At the top was a distributor plate with two inlets of diameter 3.0 mm; a liquid inlet positioned on the main axis and a gas inlet on the side. At the bottom was one central outlet of diameter 3.0 mm. This was used only for 2D images of the liquid velocity during trickle flow. The second bed was used for the 3D imaging of liquid velocity as well as for the velocity measurements on both the gas and liquid flow within the same bed. This bed was made of polyetheretherketone (PEEK) and had internal diameter 27.0 (±0.2) mm and length 100.0 cm. The arrangement of inlets and outlets was similar to the glass column. This second bed was designed for operation at pressures up to 6 bar. Both columns were filled with a random close packing of sodalime glass spheres (Jencons) with diameter 5.0 (±0.5) mm such that the column-to-sphere diameter ratios were 8 and 5.4 for the wide and narrow columns respectively. When they were mounted in the magnet bore the imaging region was 25 and 55 cm from the top of the wide and narrow columns, respectively. The Cartesian coordinate axes were defined such that positive z corresponded to the superficial flow direction. Prior to velocimetry measurements both 2D and 3D structural images of the bed were acquired, with the void space filled with water.

In all experiments the liquid was deionised water, and the temperature was constant at 22(±2) °C. The water was pumped in a closed circuit by a Verder VG330-10 gear pump and controlled by a PC-operated Bronkhorst Cori-flow (model M55C4-AAD-11-K-C) mass flow controller. When air was used as the gas phase, it was supplied from an oil-less compressor; its flow rate being measured by a rotameter and controlled by a needle valve. The outlet of the bed was at atmospheric pressure. After leaving the bed the air-water mixture entered a vessel from which the water was returned to the pump and the air was released to the atmosphere. The procedure when SF_6 (purity 99.99%, BOC) was used was similar. In this case the gas was supplied from a cylinder and stepped down to the required pressure by a regulator before passing through a rotameter (Brooks Sho-rate 1357/D2B5D1B00000) and then entering the column. The column was held at the required operating pressure by means of a needle valve at the outlet.

Prior to the imaging experiments the bed was fully wetted by operating the bed in pulsing flow for 5 min with a liquid superficial velocity, $v_{sl} = 7.6$ mm s^{-1} and a gas superficial velocity, $v_{sg} = 122.4$ mm s^{-1}. The liquid and gas superficial velocities were then set to the desired trickle flow superficial velocities. The superficial velocity is the volumetric flow rate per unit cross section area of the column and is not modified by the voidage. The Reynolds numbers, Re_i (where i = g or l, depending on whether gas or liquid flow is considered), quoted are based on the diameter of the packing elements used and the fluid superficial velocity.

For the 2D liquid velocity experiments, air was used as the gas phase; images were recorded for a constant air superficial velocity of 23.2 mm s^{-1} ($Re_g = 7.5$) with a liquid superficial velocity in the range 0.5–8.7 mm s^{-1} ($2.5 < Re_l < 43.2$). The 3D liquid velocity experiments were again performed with air and water as the gas and liquid phase, respectively. The gas and liquid superficial velocities were 52.4 and 2.3 mm s^{-1}, respectively.

For the 2D gas and liquid velocity measurements, the bed was operated at a gas pressure of 4.7 bar. The velocities of the liquid and gas phases were measured separately on the ^{1}H and ^{19}F channels respectively. Singly tuned coils were used, and therefore it was necessary to change the r.f. coil without interrupting the flow. During changeover between coils, the outlet pipe from the reactor was temporarily disconnected to allow the coil to be changed. During this period the pressure in the reactor and the superficial velocities of both fluids were kept constant. To minimise the data acquisition time for the liquid velocity map, the water was doped with Gd^{3+} ions at a concentration of 1.32 mM, giving $T_1 = 46.5$ ms, as measured by an inversion recovery pulse sequence, to reduce data acquisition times. The gas and liquid superficial velocities were 52.4 mm s^{-1} and 2.3 mm s^{-1}, respectively.

3. MRI

Experiments were performed on a Bruker Spectrospin DMX200, 4.7 T magnet equipped with shielded gradient coils providing a maximum gradient strength of 13.50 G cm^{-1}. Two birdcage coils were used of length and diameter 6.3 cm, tuned to a ^{1}H frequency of 199.7 MHz and a ^{19}F frequency of 187.9 MHz, respectively. The pulse sequences used for the 2D and 3D liquid velocimetry experiments are shown in Fig. 1. Ramped phase encode gradients and sinusoidal flow encode gradients were used to reduce slew rates and give more accurate gradient shape. The stability of the flow

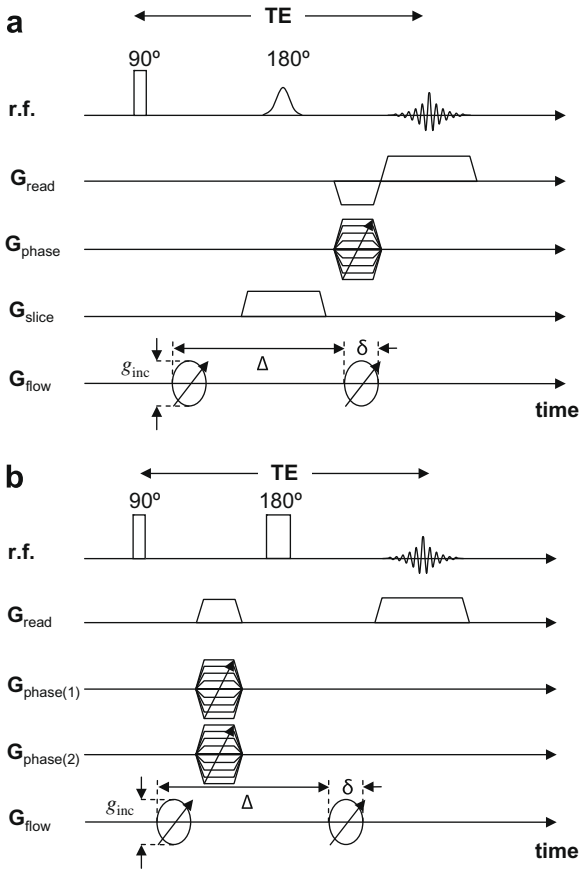

Fig. 1. Spin-echo velocity imaging pulse sequences used for (a) 2D, and (b) 3D flow velocity maps. TE is the echo time. A single velocity encode increment, i.e. two velocity encoded images, was used for the acquisition of all velocity data.

field over typical image data acquisition times was confirmed by acquiring a series of images and confirming reproducibility, to within experimental error, within the series. Three series of data were acquired: (a) 5 one-dimensional (1D) spin-echo signal intensity profiles, recorded at 1 min intervals, with a 45 mm field-of-view along the length of the bed; (b) 32 consecutive ultra-fast 2D FLASH images of the liquid distribution in the *x-y* plane; each image had an acquisition time of 122 ms and an in-plane spatial resolution of 0.7 mm × 1.4 mm; (c) Series of 5 2D liquid velocity images were acquired in the *x-y* plane; each image had an acquisition time of 68 min and an in-plane spatial resolution of 176 μm × 176 μm.

The velocity imaging data reported here were produced by correcting the phase shift measured in each voxel for the phase offset under zero-flow conditions acquired for the bed saturated with liquid. A structural image of the same field-of-view was also acquired using a spin-echo imaging sequence. This image was binary gated and then superimposed onto the liquid velocity image. In the liquid velocity image, the voxels assigned neither to glass spheres nor liquid were assigned to the gas phase.

With respect to the implementation of the liquid velocity imaging pulse sequence, parameters were selected guided by the following considerations: (i) a short observation time, Δ, as required for a short-T_2 system and also to give a nearly instantaneous velocity measurement; (ii) a velocity range only marginally greater than the distribution of velocities in the sample was employed to maximise the resolution in the velocity measurement; (iii) voxel size was minimised to reduce liquid shear across the voxel. Although shear within a voxel will still occur, the phase distribution is small compared to π and therefore the error arising from non-symmetric phase distributions will also be small.

In designing the experimental system for gas velocity imaging, consideration was given to the material used for the packing elements; sodalime and borosilicate glass spheres were considered. Sodalime spheres were selected since the smaller magnetic susceptibility variation between SF_6 and sodalime spheres gave rise to a longer T_2^* than for the SF_6-borosilicate system. No evidence of a change in T_1 as a function of time, arising from adsorption of SF_6 [16] onto the surface of the glass spheres was observed for the packing of sodalime spheres.

With respect to optimising the parameters in the velocity imaging pulse sequence for SF_6 imaging, the effect on the acquired signal of gas pressure and superficial gas velocity were examined. As expected, there was a linear increase in signal intensity with gas pressure, and the linear relationship for T_1 as a function of pressure, reported by Kuethe et al. [15], was confirmed, along with a similar linear increase in T_2 and to a lesser extent T_2^*. Whilst increasing T_1 will be associated with an increase in the required minimum recycle time, in practice this is limited by gradient duty. Hence, the increased nuclear spin density and longer T_2 values, which allowed us to use longer observation times, favoured operation at the highest gas pressures possible in the reactor.

Fig. 2 summarises the results of experiments to determine the effect of gas superficial velocity on the signal intensity. The apparent transverse relaxation time $T_{2,app}$, (or decay time) of SF_6 in the dry packed bed was measured using a Hahn echo experiment, as

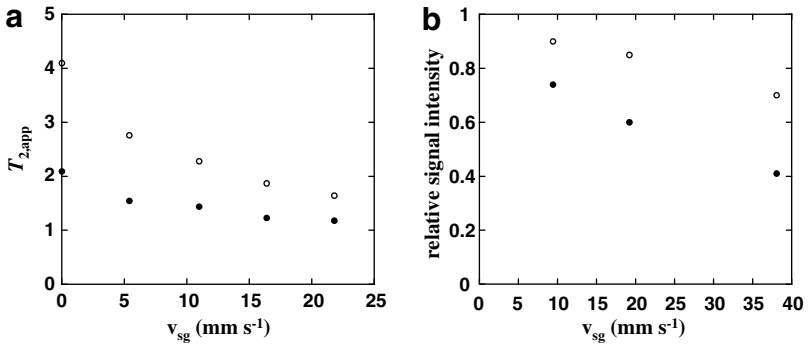

Fig. 2. Influences on the acquired signal intensity of ^{19}F in SF_6 under flowing conditions. Data are shown as a function of gas superficial velocity. (a) Decay time from a Hahn echo experiment for gas pressures of 5 (○) and 2 (●) bar. (b) The effect of observation time on relative signal intensity for a velocity imaging experiment. Data are shown for Δ, δ, TE values of 2.2 ms, 0.54 ms, 3.5 ms (○) and 3.7 ms, 0.32 ms, 4.7 ms (●). The gas pressure is 5 bar. The product $\delta\Delta g\gamma v_{sg}$ is kept constant in all experiments. Relative signal intensity has arbitrary units but all data have the same scaling. Signal decreases significantly with increasing Δ. An increased signal may be expected if the attenuation is dominated by diffusion.

a function of v_{sg} at pressures of 2 and 5 bar. $T_{2,app}$ identified in Fig. 2a is defined as the exponential curve fit to the decay of the echo height as a function of echo time. In the absence of diffusive or convective motion this would correspond to the measurement of T_2 since the dephasing due to variations in magnetic field (B_0) would be refocused. However, in the presence of molecular motion, spins do not necessarily remain in the same local field and therefore the refocusing will be imperfect and the signal decay will be more rapid than T_2 in the absence of motion. This parameter is relevant because this is the decay time that is encountered in the spin-echo velocity imaging experiment. The data shown in Fig. 2a confirm that the longer relaxation times associated with higher gas pressure are still evident as the gas velocity increases thereby making the phase shift velocity measurement more accurate at higher pressure, as a result of greater signal-to-noise in the acquired data. The observation that the data for the two gas pressures tend towards one another at high gas superficial velocities suggests that at high pressures the effect of gas velocity is more important than the gas pressure alone. This is explained by the change in dominance of T_2 and T_2^* relaxation as the velocity increases. At low values of v_{sg}, the decay is dominated by T_2 relaxation. However, as v_{sg} increases the relaxation will be increasingly influenced by motion in background gradients which is essentially independent of gas pressure. Despite this effect, even at the highest gas velocities it is still advantageous to operate at higher pressure.

Fig. 2b shows that for gas velocity imaging in a packed bed, the maximum signal-to-noise is obtained by using the shortest possible observation time, Δ. In fast-diffusing systems such as gases, it is often preferable to choose a relatively large Δ whilst keeping the velocity encoding range, given by $\delta\Delta g\gamma$, constant. This is because in the absence of acceleration, displacement arising from coherent motion scales with time whereas diffusive displacement scales with the square root of time. However, as seen from Fig. 2b, since we observe significantly more signal at shorter values of Δ, in the system under investigation here signal attenuation is dominated by flow, as opposed to diffusion, and the short decay time. For this reason we use the minimum possible observation time in a given flow imaging pulse sequence. As seen from Fig. 2b the degree of signal attenuation increases for larger values of Δ as the superficial gas velocity increases. It is also worth noting that use of a short value of Δ is favourable because it provides a more instantaneous measure of velocity, and is also required by the short $T_{2,app}$ of the system. All these factors have a significant influence on the selection of Δ, and therefore on the signal-to-noise ratio in the acquired data; the optimum value of Δ will be quite different for a fast-diffusing gas such as propane at ambient pressure.

The optimised parameters used for the various data acquisitions used here are as follows. For the 2D liquid phase velocity imaging experiments the experimental parameters were Δ = 6.2 ms and δ = 0.6 ms, giving an echo time of 9.4 ms. The velocity range was adjusted for each liquid superficial velocity studied by varying g_{inc}. A data array of 256 × 256 voxels was acquired with an isotropic field-of-view of 45 mm, giving an in-plane resolution of 176 μm × 176 μm. The slice thickness was 1 mm. The data were acquired in five blocks of four signal averages (corresponding to one iteration of the phase cycle) to enable the identification of any changes in the flow distribution during the experiment; these blocks were then added in ***k***-space to give a single image with a higher signal-to-noise ratio. Each block was obtained with a recycle time of 2 s and a total data acquisition time of 1 h 8 min.

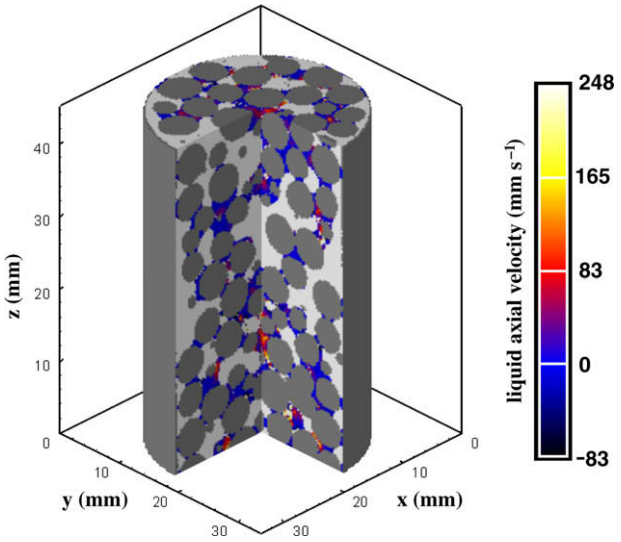

Fig. 4. 3D liquid velocity map of trickle flow with gas and liquid superficial velocities of 52.4 mm s^{-1} and 2.3 mm s^{-1}, respectively. The field-of-view was 34 mm × 34 mm × 68 mm, giving an isotropic voxel resolution of 266 μm. The bed was operated at atmospheric pressure. The packing elements and the gas-filled void space are shown as dark and light grey, respectively. (For interpretation of the references to colour in this figure legend, the reader is referred to the web version of this article.)

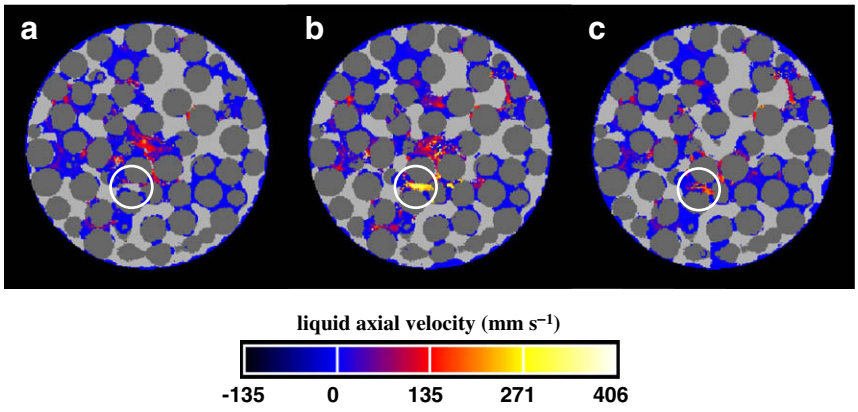

Fig. 3. 2D liquid axial velocity maps are shown for liquid superficial velocities of (a) 2.6, (b) 4.6, (c) 2.6 mm s^{-1}. The gas superficial velocity is constant at 23.2 mm s^{-1}. The highlighted region identifies a local region of the inter-particle space in which hysteresis effects in the hydrodynamics are clearly observed. Flow gradients, g_{inc}, of 2.1 and 1.4 G cm^{-1} were used for measurement of liquid superficial velocities of 2.6 and 4.6 mm s^{-1}, respectively. The isotropic field-of-view is 45 mm with in-plane resolution of 176 μm. The slice thickness is 1 mm.

For the 3D liquid velocity imaging, the 3D spin-echo velocity imaging sequence was used as shown in Fig. 1b. A data array of 128 × 128 × 256 voxels (in the *x*, *y* and *z* (read) directions respectively) was obtained with a field-of-view of 34 mm × 34 mm × 68 mm, giving an isotropic resolution of 266 μm. Eight signal averages were acquired with a recycle time of 100 ms to give a total data acquisition time of 8 h 38 min for the acquisition of a velocity map of one component of the flow velocity (i.e., v_x, v_y or v_z). The flow imaging parameters were Δ = 5 ms, δ = 1 ms and g_{inc} = 1.4 G cm^{-1}, giving a velocity range of 346 mm s^{-1} and an echo time of 6.6 ms.

The gas and liquid velocimetry experiments were performed under conditions of water-SF_6 trickle flow, with a liquid superficial velocity, v_{sl}, of 2.3 mm s^{-1} and a gas superficial velocity, v_{sg}, of 8.7 mm s^{-1} at 4.7 (±0.1) bar. For the gas velocity imaging, the spin-echo velocity imaging sequence was used with a field-of-view of 34 mm × 34 mm in a 48 × 48 data array, giving a spatial resolution of 708 μm × 708 μm. The image slice thickness was 2 mm. Values of g_{inc}, δ and Δ were 21.74 G cm^{-1}, 0.5 ms and 3.00 ms, respectively. The recycle time was 100 ms. To produce the final image 768 scans were taken giving a total data acquisition time of 30 min. For the liquid velocity imaging, a field-of-view of 34 mm × 34 mm was again used, in a 192 × 192 data array, giving a spatial resolution of 177 μm × 177 μm. The image slice thickness was 1 mm. Values of g_{inc}, δ and Δ were 4.08 G cm^{-1}, 1 ms and 2.73 ms, respectively. The recycle time was 250 ms. 16 scans were signal averaged, giving a total data acquisition time of 10.5 min. The echo time used for both the gas and liquid imaging data acquisition was 5.7 ms.

The accuracy of the velocity data was assessed by comparing superficial liquid mass balances from the MRI data with values measured macroscopically by the mass flow controller. Gas and liquid flow rates were in agreement with the macroscopic measurements to within 5% and 7%, respectively.

4. Results and discussion

Fig. 3 shows trickle flow velocity maps for the bed operating at a constant v_{sg} = 23.2 mm s^{-1} and values of v_{sl} = 2.6, 4.6 and 2.6 mm s^{-1}; these three images correspond to a time series where the liquid velocity has been increased from 2.6 to 4.6 mm s^{-1} and then decreased back to 2.6 mm s^{-1}. The heterogeneity of the flow field is clearly seen. In particular, much of the liquid holdup is stagnant but there are a number of distinct high-speed liquid channels. This is a direct visualisation of the phenomenon termed maldistribution or "uneven irrigation" [17]. As the liquid superficial velocity increases, the predominant means by which the extra flow is carried appears to be that extra rivulets emerge, rather than an increase in the velocities of the existing rivulets. The velocity maps also reveal a significant degree of irreproducibility and hysteresis of the flow field, with a different local flow pattern being established on returning to the same superficial velocity. Hysteresis had previously been observed by liquid holdup measurements using MRI [18] and X-ray CT [19], but the additional velocity information emphasises the variation in the flow field even further. This behaviour is in contrast to single-phase flow where it is now generally accepted that the flow field is reproducible at low Reynolds numbers [20].

Fig. 4 is a 3D visualisation of the *z*-component of the velocity field; heterogeneity of the liquid distribution and flow field is clearly seen. Fig. 5 shows a visualisation of the three components of the velocity field. The colour and magnitude of the vectors both show the speed with which the liquid is flowing; the direction of

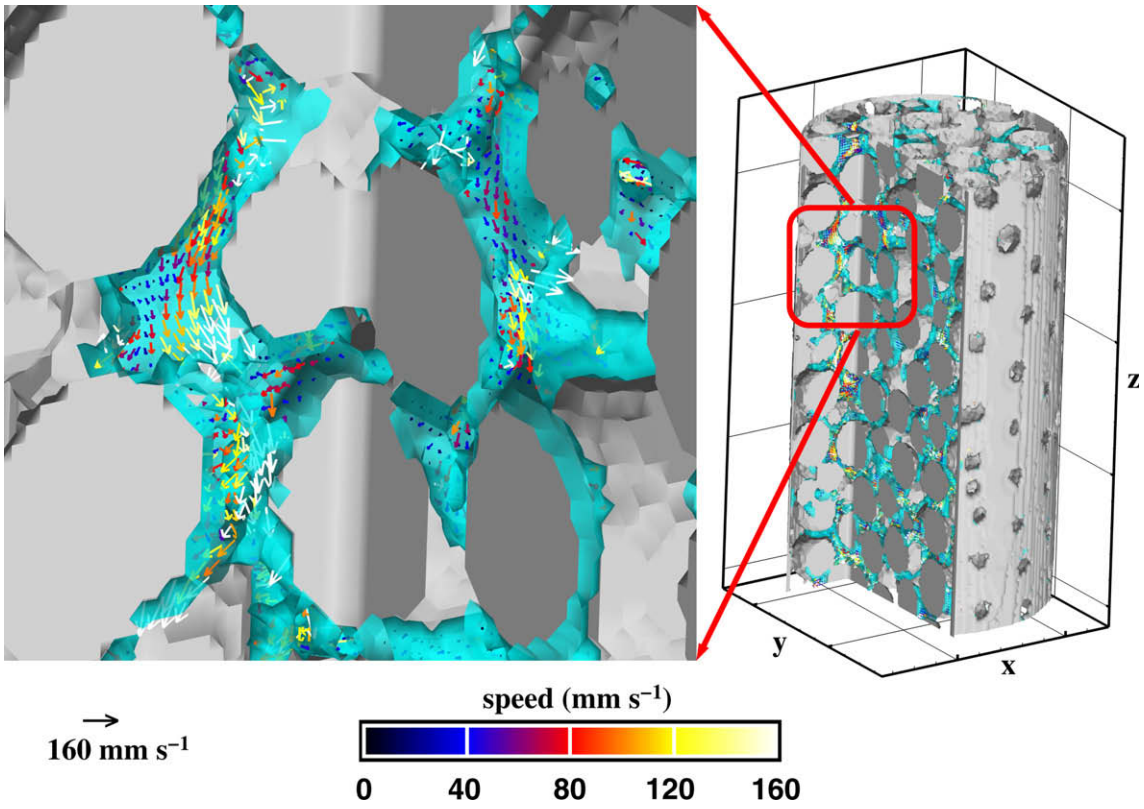

Fig. 5. 3D visualisation of the v_x, v_y, v_z components of the liquid flow field during trickle flow. The gas and liquid superficial velocities are 52.4 mm s^{-1} and 2.3 mm s^{-1}, respectively. The field-of-view was 34 mm × 34 mm × 68 mm, giving an isotropic voxel resolution of 266 μm. The bed was operated at atmospheric pressure. Packing elements are shown as grey; the gas is not shown (transparent). The liquid-filled regions of the bed are identified as light blue. The flow vectors identify the direction and magnitude of the flow. For clarity, the magnitude is also colour-coded according to the colour scale shown. (For interpretation of the references to colour in this figure legend, the reader is referred to the web version of this article.)

the arrow indicates the direction of flow. The distribution of the v_z component of velocity is shown in Fig. 6. The distributions for v_x and v_y are identical, centred on zero and symmetric with velocities up to ±150 mm s^{-1}; i.e., reaching maximum values at $\sim 50 v_{sl}$, as opposed to $\sim 5 v_{sl}$ observed for single-phase flow [4]. The axial velocity distribution has three main features: (i) a pronounced peak at zero velocity, (ii) a very long positive tail, and (iii) a considerable degree of reverse flow. The peak at zero is due to the existence of stagnant regions and the no-slip boundary condition at solid surfaces; it is noticeably sharper than the equivalent for single-phase flow, indicating proportionally more stagnant fluid. The positive tail illustrates the heterogeneity of the flow field with the fastest-flowing regions having velocities of up to $100 v_{sl}$, an order of magnitude greater than those in single-phase flow. This is consistent with observation of Shah and Sharma [21] that the axial dispersion in the liquid phase under trickle flow conditions can be an order of magnitude higher than in the single phase. The distribution of positive velocities fits a double-exponential curve in contrast to single-phase flow which can be described by a single-exponential function [4,22]. The origin of the double-exponential curve is tentatively assigned to two distinct hydrodynamic regions in the flow; the higher velocities (slow exponential decay) corresponding to rivulet (large channel) flow and the low velocities to film flow. These data also report the first direct visualisation of back-flow in trickle-beds, although it has been inferred from residence-time distribution measurements [23]. Back-flow has been consistently observed in single-phase flow [22,24–26] and has been attributed to circulating flow patterns in the immediate vicinity of surfaces or vortex-like structures at the meeting points of stream lines. The ratio of reverse to positive flow in the present trickle flow data is ~0.2 which is much greater than the equivalent value for single-phase flow (generally 0.01–0.05).

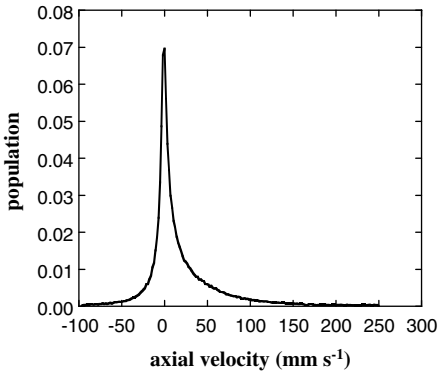

Fig. 6. Axial velocity distribution of liquid during two-phase trickle flow. The operating conditions of the bed are as described in Fig. 4. Population refers to the fraction of image voxels containing liquid associated with a given axial velocity.

Fig. 7 shows separate axial velocity maps of (a) the liquid phase and (b) the gas phase during uninterrupted water-SF_6 trickle flow with v_{sl} = 2.3 mm s^{-1} and v_{sg} = 8.7 mm s^{-1} at P = 4.7 bar. In each case the regions occupied by the other fluid phase and the solid spheres appear black, representing the absence of signal. The data were zero-filled in the x and y directions to 256 × 256 to produce the liquid and gas velocity maps shown. The gas flow field is compared with (c) single-phase liquid flow at v_{sl} = 8.7 mm s^{-1}. Gas exists in regions of the bed occupied by the fastest-moving liquid in single-phase liquid flow. The separate liquid and gas velocity maps were superimposed to give a combined velocity map of both phases in trickle flow (Fig. 8). Inspection of Fig. 8 reveals that the regions of highest gas velocity are in the centre of pores which are primarily gas-filled. The regions of high liquid velocity tend to be in pores that are primarily liquid-filled. Most interestingly, from the point of view of giving insights for numerical simulation, the gas and liquid velocities at a gas–liquid interface also appear to be heterogeneous in nature. At some interfaces the interfacial velocities are near stagnant for both phases but there are also examples where high velocity liquid appears adjacent to quite slowly moving gas. In ongoing studies we are using these gas–liquid velocity maps to measure directly values of gas and liquid velocity across the gas–liquid interface that exists within the void space between the glass spheres comprising the bed. This information will be used to identify the appropriate closure law for use in numerical simulations; e.g. computational fluid dynamics.

5. Conclusions

The numerical modelling of two-phase flow within porous structures, such as bead packs or fixed-bed reactors, requires the use of relationships which, for example, relate the gas and liquid flow fields. This paper reports the implementation of gas and liquid velocity imaging of stable, two-phase flow such that quantitative flow velocity maps are achieved, with sufficient spatial resolution,

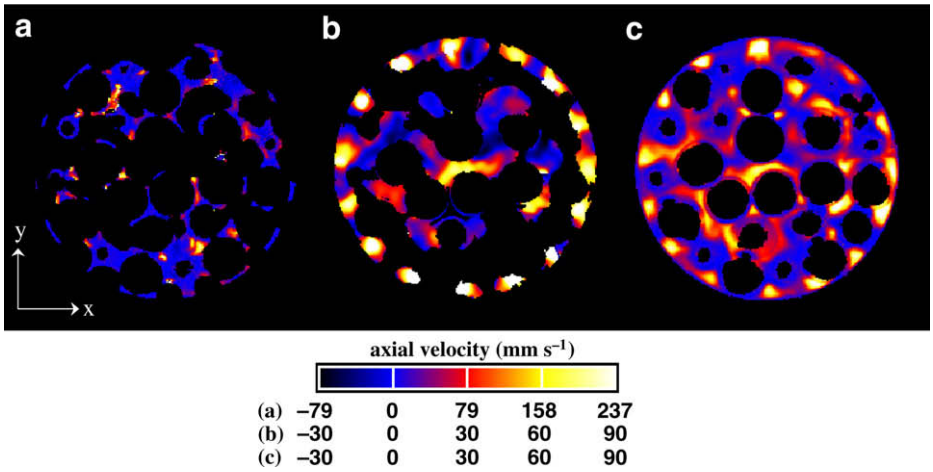

Fig. 7. Axial velocity maps of (a) liquid (water) during trickle flow; (b) gas (SF_6) during trickle flow; (c) liquid (water) in single-phase flow. The superficial velocities of the gas and liquid in trickle flow were 8.7 mm s^{-1} and 2.3 mm s^{-1}, respectively at a pressure of 4.7 bar. The superficial velocity of the liquid phase in (c) was the same as the gas phase in (a) and (b). The field-of-view was 34 mm × 34 mm, giving acquired isotropic resolutions of (a) and (c) 177 μm, (b) 708 μm. The slice thicknesses were (a) 1 mm, (b) 2 mm, (c) 2 mm. The data were zero-filled as described in the text.

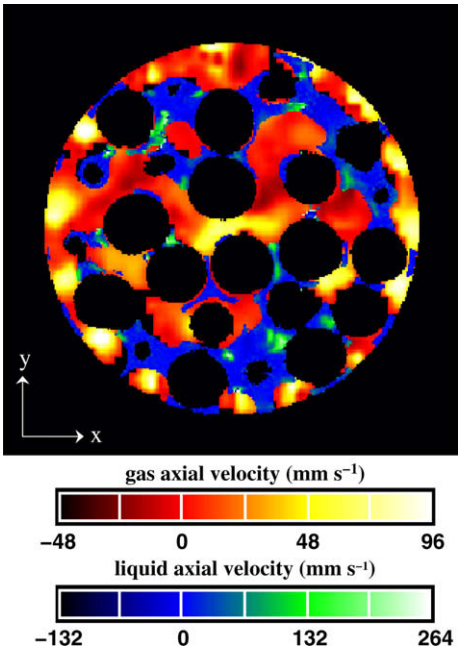

Fig. 8. Gas and liquid velocity map of SF_6 (red/yellow) and water (blue/green) during trickle flow. The gas and liquid superficial velocities were 8.7 mm s^{-1} and 2.3 mm s^{-1}, respectively. The bed was operated at a pressure of 4.7 bar. (For interpretation of the references to colour in this figure legend, the reader is referred to the web version of this article.)

that it is now possible to image liquid and gas velocity maps within local elements of the void space between adjacent packing elements (i.e., glass spheres) comprising the bed. These data can now be used to critically consider the methods currently used in numerical simulation of two-phase flows in porous media.

Acknowledgments

MHS acknowledges the University of Cambridge and Trinity College, Cambridge for financial support. AJS and LFG also acknowledge support from EPSRC Grants GR/S43719/01 and GR/S20789/01.

References

[1] M.H. Al-Dahhan, F. Larachi, M.P. Duduković, A. Laurent, High-pressure trickle-bed reactors: a review, Ind. Eng. Chem. Res. 36 (1997) 3292–3314.
[2] A. Attou, C. Boyer, Hydrodynamics of gas–liquid–solid trickle-bed reactors: a critical review, Oil Gas Sci. Technol. 54 (1999) 29–66.
[3] A.J. Sederman, L.F. Gladden, Magnetic resonance imaging as a quantitative probe of gas–liquid distribution and wetting efficiency in trickle-bed reactors, Chem. Eng. Sci. 56 (2001) 2615–2628.
[4] A.J. Sederman, L.F. Gladden, Magnetic resonance visualisation of single- and two-phase flow in porous media, Magn. Reson. Imaging 19 (2001) 339–343.
[5] M.D. Mantle, A.J. Sederman, L.F. Gladden, Single- and two-phase flow in fixed-bed reactors: MRI flow visualisation and lattice-Boltzmann simulations, Chem. Eng. Sci. 56 (2001) 523–529.
[6] L.F. Gladden, M.H.M. Lim, M.D. Mantle, A.J. Sederman, E.H. Stitt, MRI visualisation of two-phase flow in structured supports and trickle-bed reactors, Catal. Today 79 (2003) 203–210.
[7] N.L. Nguyen, V. van Buren, A. von Garnier, E.H. Hardy, R. Reimert, Application of magnetic resonance imaging (MRI) for investigation of fluid dynamics in trickle bed reactors and of droplet separation kinetics in packed beds, Chem. Eng. Sci. 60 (2005) 6289–6297.
[8] M.H.M. Lim, A.J. Sederman, L.F. Gladden, E.H. Stitt, New insights to trickle and pulse flow hydrodynamics in trickle-bed reactors using MRI, Chem. Eng. Sci. 59 (2004) 5403–5410.
[9] L.F. Gladden, L.D. Anadon, M.H.M. Lim, A.J. Sederman, E.H. Stitt, Insights into the mechanism of the trickle-to-pulse transition in trickle-bed reactors, Ind. Eng. Chem. Res. 44 (2005) 6320–6331.
[10] L.D. Anadon, A.J. Sederman, L.F. Gladden, Mechanism of the trickle-to-pulse transition in fixed-bed reactors, A.I.Ch.E. J. 52 (2006) 1522–1532.
[11] I.V. Koptyug, S.A. Altobelli, E. Fukushima, A.V. Matveev, R.Z. Sagdeev, Thermally polraized ^{1}H NMR microimaging studies of liquid and gas flow in monolithic catalysts, J. Magn. Reson. 147 (2000) 36–42.
[12] B. Newling, C.C. Poirier, Y. Zhi, J.A. Rioux, A.J. Coristine, D. Roach, B.J. Balcolm, Velocity imaging of highly turbulent gas flow, Phys. Rev. Lett. 93 (2004). Art. No. 154503.
[13] S.D. Beyea, S.A. Altobelli, L.A. Monday, Chemically selective NMR imaging of a 3-component (solid-liquid-liquid) sedimenting system, J. Magn. Reson. 161 (2003) 198–203.
[14] A. Boushehri, J. Bzowski, J. Kestin, E.A. Mason, Equilibrium and transport properties of 11 polyatomic gases at low density, J. Phys. Chem. Ref. Data 16 (1987) 445–466.
[15] D.O. Kuethe, T. Pietrass, V.C. Behr, Inert fluorinated gas T_1 calculator, J. Magn. Reson. 177 (2005) 212–220.
[16] A. Caprihan, C.F.M. Clewett, D.O. Kuethe, E. Fukushima, S.J. Glass, Characterization of partially sintered ceramic powder compacts using fluorinated gas NMR imaging, Magn. Reson. Imaging 19 (2001) 311–317.
[17] S.T. Sie, R. Krishna, Process development and scale up: III. Scale-up and scale-down of trickle bed processes, Rev. Chem. Eng. 14 (1998) 203–252.
[18] A.J. Sederman, MRI studies of single- and multi-phase flow in porous media, Ph.D. Thesis, University of Cambridge, 1998.
[19] W. van der Merwe, W. Nicol, F. de Beer, Trickle flow distribution and stability by X-ray radiography, Chem. Eng. J. 132 (2007) 47–59.
[20] M.L. Johns, A.J. Sederman, A.S. Bramley, L.F. Gladden, P. Alexander, Local transitions in flow phenomena through packed beds identified by MRI, A.I.Ch.E. J. 46 (2000) 2151–2161.
[21] Y.T. Shah, M.M. Sharma, Gas–liquid–solid reactors, in: J.J. Carberry, A. Varma (Eds.), Gas–Liquid–Solid Reactors in Chemical Reaction and Reactor Engineering, Marcel Dekker Inc., New York, 1986, pp. 667–734.
[22] Y.E. Kutsovsky, L.E. Scriven, H.T. Davis, B.E. Hammer, NMR imaging of velocity profiles and velocity distributions in bead packs, Phys. Fluids 8 (1996) 863–871.
[23] K.D.P. Nigam, I. Iliuta, F. Larachi, Liquid back-mixing and mass transfer effects in trickle-bed reactors filled with porous catalyst particles, Chem. Eng. Process. 41 (2002) 365–371.
[24] A.J. Sederman, M.L. Johns, P. Alexander, L.F. Gladden, Structure-flow correlations in packed beds, Chem. Eng. Sci. 53 (1998) 2117–2128.
[25] J. Gotz, K. Zick, C. Heinen, T. Konig, Visualisation of flow processes in packed beds with NMR imaging: determination of the local porosity, velocity vector and local dispersion coefficients, Chem. Eng. Process. 41 (2002) 611–629.
[26] X.H. Ren, S. Stapf, B. Blümich, Magnetic resonance visualisation of flow and pore structure in packed beds with low aspect ratio, Chem. Eng. Technol. 28 (2005) 219–225.